International Journal of Nanomedicine Dovepress

Open Access Full Text Article ORIGINAL RESEARCH

Augment of Ferroptosis with Photothermal Enhanced Fenton Reaction and Glutathione Inhibition for Tumor Synergistic Nano-Catalytic Therapy

Qingcheng Song[1,2,*], Yiran Zhang[3,*], Hongzhi Hu[4,*], Xuemei Yang[5], Xin Xing[1,2], Jianhua Wu[6], Yanbin Zhu[1,2], Yingze Zhang[1,2]

[1]Department of Orthopaedic Surgery, Third Hospital of Hebei Medical University, Shijiazhuang, Hebei, People's Republic of China; [2]Orthopaedic Institution of Hebei Province, Shijiazhuang, Hebei, People's Republic of China; [3]School of Medicine, Nankai University, Tianjin, People's Republic of China; [4]Department of Orthopedics, Union Hospital, Tongji Medical College, Huazhong University of Science and Technology, Wuhan, Hubei, People's Republic of China; [5]The Fourth Hospital of Shijiazhuang, Shijiazhuang, Hebei, People's Republic of China; [6]The Fourth Hospital of Hebei Medical University, Shijiazhuang, Hebei, People's Republic of China

*These authors contributed equally to this work

Correspondence: Yingze Zhang; Yanbin Zhu, Email yzling_liu@163.com; 38600312@hebmu.edu.cn

Introduction: Ferroptosis-driven tumor ablation strategies based on nanotechnology could be achieved by elevating intracellular iron levels or inhibiting glutathione peroxidase 4 (GPX4) activity. However, the intracellular antioxidative defense mechanisms endow tumor cells with ferroptosis resistance capacity. The purpose of this study was to develop a synergistic therapeutic platform to enhance the efficacy of ferroptosis-based tumor therapy.

Methods: In this study, a multifunctional nano-catalytic therapeutic platform (mFeB@PDA-FA) based on chemodynamic therapy (CDT) and photothermal therapy (PTT) was developed to effectively trigger ferroptosis in tumor. In our work, iron-based mesoporous Fe_3O_4 nanoparticles (mFe_3O_4 NPs) were employed for the encapsulation of L-buthionine sulfoximine (BSO), followed by the modification of folic acid-functionalized polydopamine (PDA) coating on the periphery. Then, the antitumor effect of mFeB@PDA-FA NPs was evaluated using Human OS cells (MNNG/HOS) and a subcutaneous xenograft model of osteosarcoma.

Results: mFe_3O_4 harboring multivalent elements ($Fe^{2+/3+}$) could catalyze hydrogen peroxide (H_2O_2) into highly cytotoxic $^{\cdot}OH$, while the tumor microenvironment (TME)-responsive released BSO molecules inhibit the biosynthesis of GSH, thus achieving the deactivation of GPX4 and the enhancement of ferroptosis. Moreover, thanks to the remarkable photothermal conversion performance of mFe_3O_4 and PDA shell, PTT further synergistically enhanced the efficacy of CDT and facilitated ferroptosis. Both in vivo and in vitro experiments confirmed that this synergistic therapy could achieve excellent tumor inhibition effects.

Conclusion: The nanotherapeutic platform mFeB@PDA-FA could effectively disrupted the redox homeostasis in tumor cells for boosting ferroptosis through the combination of CDT, PTT and GSH elimination, which provided a new perspective for the treatment of ferroptosis sensitive tumors.

Keywords: ferroptosis, chemodynamic therapy, photothermal therapy, Fenton reaction, BSO

Introduction

Osteosarcoma (OS) is the most common primary malignant bone tumor and the leading cause of cancer-related death in children and adolescents.[1,2] At present, the common treatment methods of OS are surgical resection, systemic chemotherapy and radiotherapy, but the therapeutic approaches are far from satisfactory due to chemotherapy resistance and postoperative distant metastasis.[3–5] Hence, the development of new strategies that combine biomedicine with emerging nanotechnology to find alternative ways to stimulate cell death may overcome the current therapeutic dilemma.[6]

Ferroptosis, as a non-apoptotic form of programmed cell death, has received considerable attention due to its unique properties associated with various diseases, including cancer.[7,8] Different from traditional apoptosis and necrosis,

Received: 30 May 2024
Accepted: 23 October 2024
Published: 16 November 2024

Graphical Abstract

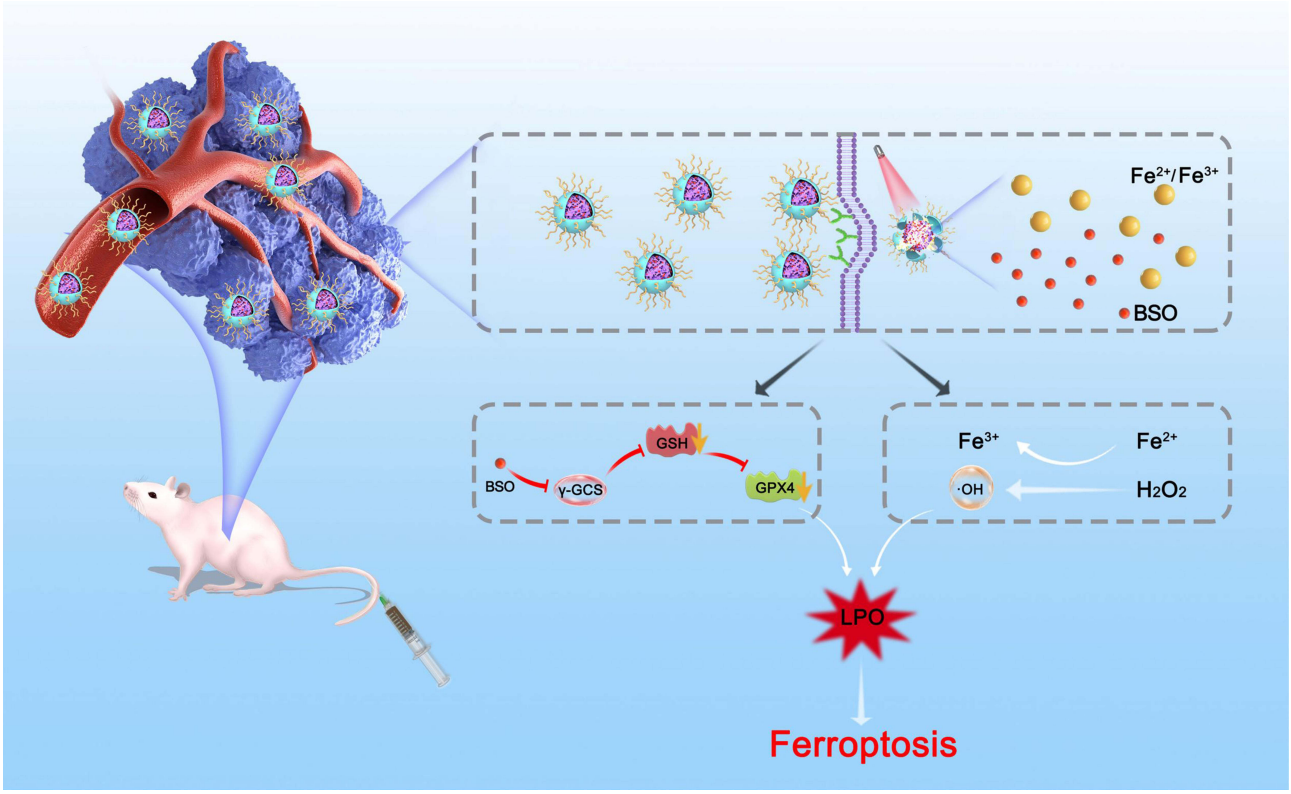

ferroptosis is mainly characterized by iron-dependent ROS generation and lipid peroxidation (LPO), which is of great significance for killing tumor cells resistant to necrosis and apoptosis.[9,10] Therefore, the intracellular redox active iron (Fe^{2+}) level is the key elements in the process of inducing ferroptosis, which could catalyze the decomposition of hydrogen peroxide (H_2O_2) in the tumor microenvironment (TME) to generate highly toxic hydroxyl radicals ($^{\cdot}OH$) based on Fenton reaction and promote the accumulation of lipid peroxides, thus causing damage to the structure and integrity of tumor cells.[11–13] Thus, ferroptosis is expected to provide new treatment opportunities for cancers that are resistant to traditional therapies.

Of note, many studies have demonstrated that ferroptosis could inhibit the invasion and proliferation of OS to a large extent.[14–16] Importantly, with the rapid development of nanotechnology in the field of biomedicine, a large number of iron-based nanomaterials have been designed to initiate the intracellular Fenton reaction to induce the intracellular generation of ROS and LPO.[17–19] However, at high levels of intracellular GSH, tumor cells could use glutathione peroxidase 4 (GPX4) to convert lipid peroxides into non-toxic lipid alcohols, thereby protecting themselves from the effect of ferroptosis.[20–22] In view of this, the inhibition of GPX4 activity or reduction of intracellular GSH levels while effectively delivering iron is expected to achieve effective ferroptosis in tumor cells. However, achieving this enhanced ferroptosis through amorphous iron nanoparticles present huge challenge due to their insufficient catalytic efficiency and limited drug delivery capacity. For this purpose, it is imperative to construct a multifunctional nano-catalysis treatment platform which can not only act as an iron donor to initiate Fenton reaction, but also inhibit GPX4 activity or consume GSH to effectively induce ferroptosis in tumor cells.

Considering the critical role of iron in inducing ferroptosis in tumor cells, a kind of iron oxide nanoparticles with mesoporous structure (mFe_3O_4 NPs) has received extensive attention due to its surface effect and quantum size effect similar to ordinary nanomaterials, as well as its excellent drug loading capability and biosafety.[23,24] In the slightly acidic

tumor microenvironment, mFe_3O_4 could release Fe ions, which could catalyze the high concentration of H_2O_2 in TME to generate ·OH in Fenton reaction, resulting in the generation of ROS and the occurrence of ferroptosis. In addition, the released Fe^{3+} could deplete intracellular GSH for enhanced ROS accumulation, however, this process is easily compensated by the continuous synthesis of GSH.[25,26] In order to inhibit the powerful antioxidant defense system of tumor cells, a small molecule L-Buthionine-sulfoximine (BSO) was utilized as an inhibitor of γ-glutamylcysteine synthase (γ-GCS), a key enzyme involved in GSH biosynthesis pathway, which could block the replenishment of GSH, leading to the inactivation of GPX4 and the accumulation of lipid peroxides.[27–29] Based on the above consideration, it is reasonable to believe that the depletion of intracellular GSH by BSO delivered by mFe_3O_4 would be a promising strategy to disrupt intracellular redox homeostasis, leading to enhanced-ferroptosis for tumor therapy.

In this contribution, a multifunctional nano-catalytic therapeutic platform was prepared to achieve enhanced-ferroptosis in tumor treatment modality by simultaneously modulating tumor redox environment and enhancing ROS and lipid peroxides generation. In our work, biocompatible mFe_3O_4 NPs with fascinating surface area value and drug loading capacity were utilized as the core of Fenton reaction to achieve the persistent transformation of H_2O_2 to ·OH and the loading of BSO. Furthermore, in order to avoid undesirable premature release of drug molecules in the blood circulation system and endow the nanoplatform with precise targeting capacity, the surface of the drug-loading nanoplatform was subsequently coated with folic acid (FA)-functionalized polydopamine (PDA) film (mFe_3O_4/BSO@PDA-FA, denoted as mFeB@PDA-FA). As a kind of nanomaterials that can be deposited on various substrates via oxidative polymerization, PDA could further improve the physiological stability of the nanoplatform and prevent the oxidation of mFe_3O_4 NPs, thus maintaining the stable occurrence of Fenton reaction in tumors. Interestingly, the intense absorption of PDA and mFe_3O_4 in the NIR region is expected to make mFeB@PDA-FA an ideal photothermal agent for tumor ablation, while accelerating the Fenton reaction velocity by increasing the temperature of the tumor region, thus exhibiting ideal synergism with ferroptosis. Moreover, the folate receptor (FOLR) is a cell surface receptor overexpressed in multiple tumor types. Therefore, the PDA-coated nanoparticles can be further modified by FA to enhance the iron delivery ability of mFeB@PDA-FA to tumor cells.[30–32] As shown in Scheme 1, the nanoplatform could accumulate in tumor tissue and be effectively endocytosed by tumor cells through the enhanced permeability and retention (EPR) effect and FA active targeting effect. Then, the PDA coating was destroyed in the slightly acidic tumor microenvironment and resulted in the sustained release of BSO in the cytoplasm, while the exposed mFe_3O_4 could catalyze H_2O_2 to produce abundant ·OH and cause severe LPO. Simultaneously, the local hyperthermia generated by the mFeB@PDA-FA under the irradiation of 808 nm laser significantly improved the efficiency of CDT. Collectively, our study innovatively integrates the strategies of mFe_3O_4-supported drug loading and iron ion release, BSO-mediated inhibition of GSH synthesis and the enhanced photothermal effect induced by the combination of PDA and mFe_3O_4, thus effectively promoting ferroptosis through multi-pathway synergistic effects.

Materials and Methods

Materials

Iron (III) chloride hexahydrate ($FeCl_3·6H_2O$), ethylene glycol (EG), sodium acetate, dopamine hydrochloride, L-buthionine sulfoximine (BSO, ≥ 97.0%) and 2.7-dichlorofluorescein diacetate (DCFH-DA) were purchased from Sigma-Aldrich. JC-1 staining kit, calcein-AM/propidium iodide (PI) staining kit were obtained from Beyotime Biotechnology. All chemicals were of analytical grade and were used without further purification.

The Human OS cells (MNNG/HOS), bone marrow stromal cells (BMSCs) and human umbilical vein endothelial cell line cells (HUVECs) were obtained from the cell bank of Chinese Academy of Sciences (Shanghai, China).

Synthesis of mFe_3O_4 NPs

Monodispersed mFe_3O_4 NPs were synthesised according to a previously reported hydrothermal method.[33] Briefly, $FeCl_3·6H_2O$ (1 g), sodium acetate (3 g) and sodium citrate dehydrate (0.6 g) were dissolved in EG (40 mL) under intense agitation to form a homogenous mixture. Afterwards, the mixed solution was transferred to a Teflon-lined stainless steel autoclave, heated to 200 °C and reacted for 8 h. The autoclave was then cooled to ambient temperature, the product was

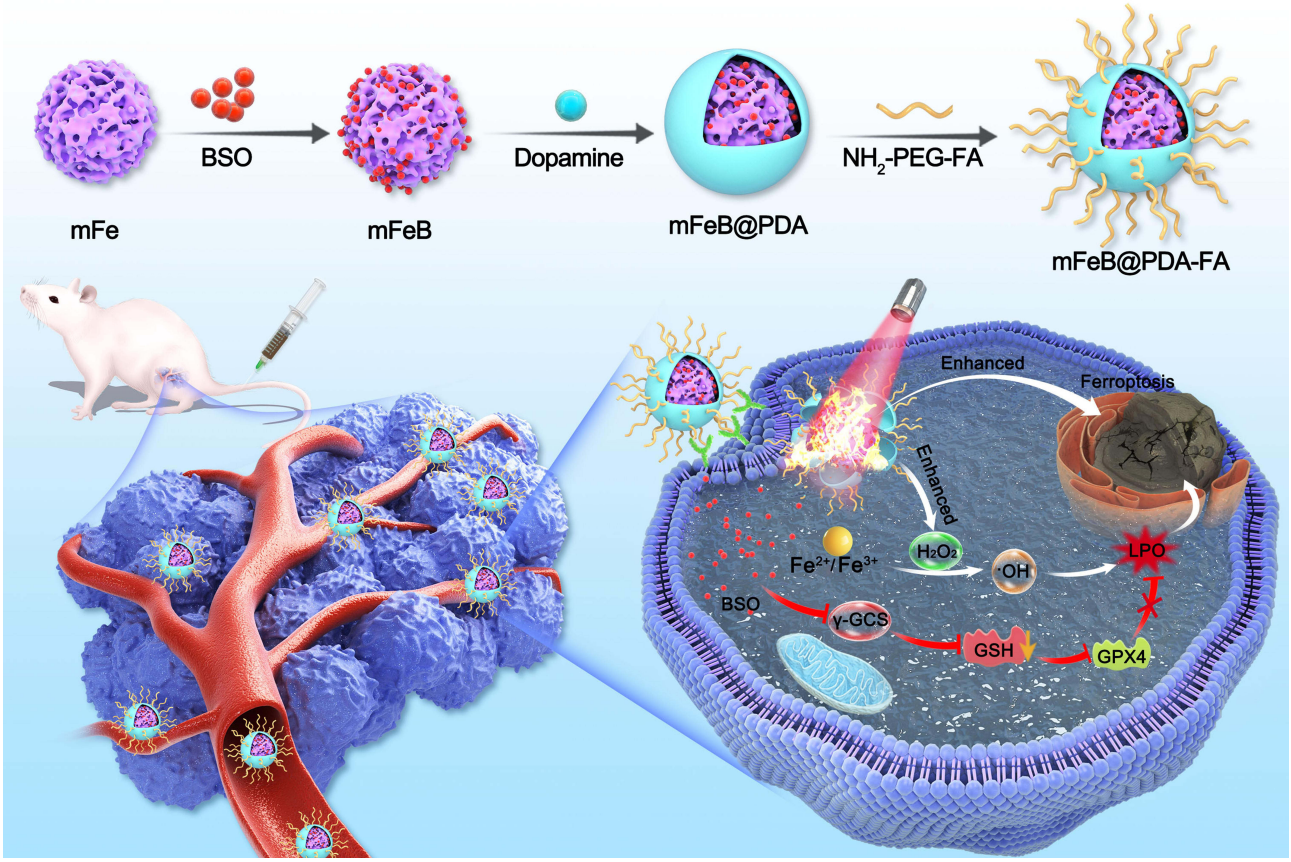

Scheme 1 Schematic illustration of the synthetic procedures of the mFeB@PDA-FA NPs with photothermal-enhanced chemodynamic process and glutathione inhibition for synergistic antitumor therapy.

collected and washed with deionized (DI) water and ethanol. The obtained mFe_3O_4 NPs were dispersed in DI water for subsequent use.

Synthesis of mFe_3O_4/BSO@PDA-FA NPs

In order to successfully implement the BSO loading, 5 mg of BSO was dispersed in 20 mL DI water containing 10 mg mFe_3O_4 NPs. The mixed solution was stirred at room temperature for 24 h and the precipitate was collected by centrifugation at 12000 rpm for 10 min, followed by gently washing 3 times with DI water to remove the free BSO. The yielded mFe_3O_4/BSO NPs were then dried with lyophilization and stored at 4 °C before further use.

The coating of PDA shell was achieved by a previously reported solution oxidation method.[34,35] In brief, the synthesized mFe_3O_4/BSO NPs were dissolved in 40 mL Tris buffer solution (pH 8.5, 10 mM) containing 20 mg dopamine hydrochloride and stirred overnight at room temperature. Afterwards, the resultant product was isolated with a magnet followed by gently washing twice with DI water and then dried with lyophilization to obtain mFe_3O_4 /BSO@PDA NPs (mFeB@PDA NPs).

To achieve the successful grafting of FA on the surface of the PDA shell, 10 mg of mFeB@PDA NPs and 10 mg of NH_2-PEG-FA were dissolved in 10 mL Tris buffer solution (pH 8.5, 10 mM) and stirred at room temperature for 6 h. After reaction, the resulting product was magnetically separated and washed with DI water to remove residual reactants and mFe_3O_4/BSO@PDA-FA NPs (mFeB@PDA-FA NPs) were obtained after lyophilization. The non-FA-grafted mFe_3O_4/BSO@PDA NPs were synthesised by following a similar protocol apart from replacing NH_2-PEG-FA with NH_2-PEG.

Characterizations

The morphology of the synthesised nanoparticles was observed by transmission electron microscopy (TEM, JEOL 2100F, Japan) and scanning electron microscopy (SEM, ZEISS, Gemini 300). The valence of Fe element in mFe_3O_4 NPs was analyzed by X-ray photoelectron spectroscopy (XPS). The surface area and mesoporous structure of mFe_3O_4 NPs were detected by Brunauer-Emmett-Teller (BET) method. The zeta potential and hydrodynamic size were investigated by a Zetasizer Nano ZS system (Malvern, UK). The generation of ˙OH in different reaction systems was detected by an electron spin resonance (ESR) spectrometer (Bruker Germany).

In vitro Photothermal Performance

The in vitro photothermal performance of mFeB@PDA-FA was investigated by 808 nm laser irradiation. Different concentrations of mFeB@PDA-FA suspensions were irradiated with an 808 nm laser and the real-time temperature was recorded every 30 seconds using an infrared thermal imaging camera (Testo 865, Testo, Schwarzwald, Germany). The laser power density-dependent photothermal properties of mFeB@PDA-FA were further investigated by irradiating mFeB@PDA-FA suspension with different laser power densities (0.5, 1.0, 1.5, 2.0 W cm^{-2}). In order to explore the thermal stability of NPs, mFeB@PDA-FA suspension was irradiated with 808 nm NIR laser (1.0 W cm^{-2}) for five cycles and the temperature changes of suspension was measured. Furthermore, mFeB@PDA-FA suspension with a concentration of 200 μg mL^{-1} was irradiated with 808 nm laser and the temperature changes during the heating and natural cooling phases were monitored. The photothermal conversion efficiency was calculated according to the following formula:

$$\eta = \frac{hS(T_{max} - T_{surr}) - Q_{dis}}{I\left(1 - 10^{-A_\lambda}\right)} \tag{1}$$

where h represents heat transfer coefficient, S is the surface area of the vessel, T_{max} is the maximum temperature of the sample solution, T_{surr} is the surrounding temperature, the power density of 808 nm laser and the absorption value of the sample solution at wavelength 808 nm are denoted as I and A_λ, respectively. Q_{dis} represents the heat loss from the light absorption of the quartz sample cell itself.

Evaluation of Michaelis-Menten Kinetics

A typical TMB colorimetric analysis was conducted to evaluate the Fenton reaction activity of mFe_3O_4 NPs. Briefly, the mFe_3O_4 NPs (100 μg mL^{-1}) and TMB (1 mM, 1 mL) were added to PBS solution (pH 5.5) containing 5 mm H_2O_2 and reacted at different temperatures (25 °C, 45 °C) for 10 min. The absorbance of different reaction systems was measured by UV-vis absorption spectroscopy. Furthermore, the steady-state kinetic assays of mFe_3O_4 NPs were investigated by monitoring the absorbance change of TMB at 652 nm with different concentrations of H_2O_2 (5, 10, 20, 50 mM) as substrate. The corresponding initial velocities (v_0) of ˙OH production were calculated by the Beer-Lambert law (Eq (2), ε =39000M^{-1} cm^{-1}, l = 10 mm) and the Michaelis-Menten kinetic curves were obtained by plotting v_0 against the corresponding H_2O_2 concentrations (Eq (3)). Furthermore, the Michaelis-Menten constant (K_m) and maximum reaction velocity (V_{max}) were determined according to a linear double reciprocal plot (Lineweaver-Burk plot, (Eq (4)).

$$A = \varepsilon lc \tag{2}$$

$$v_0 = \frac{V_{max} \cdot [S]}{K_m + [S]} \tag{3}$$

$$\frac{1}{v_0} = \frac{K_m}{V_{max}} \cdot \frac{1}{[S]} + \frac{1}{V_{max}} \tag{4}$$

Detection of Intracellular Oxidation Levels

For intracellular GSH level detection, the MNNG/HOS cells were seeded into 6-well plate (1×10^5 cells per well) and cultured overnight at 37 °C. Subsequently, the cells were treated with different formulations for 6 h: (1) control, (2)

mFe_3O_4, (3) mFeB@PDA-FA, (4) mFeB@PDA-FA + NIR. Then, the cells were harvested and the cellular GSH content of each group was detected using a glutathione assay kit according to the manufacturer's protocol. The percentage of GSH in each group was obtained by comparing with that in the untreated cells. For the detection of intracellular LPO generation, the MNNG/HOS cells were inoculated into a 6-well plate at a density of 1×10^5 cells per well and incubated overnight. After receiving different treatments, the LPO level in each group was evaluated by measuring MDA content through a LPO MDA assay kit according to established methods.[36]

Cellular Uptake Experiments

The cellular uptake behavior was monitored using an inverted fluorescence microscope. MNNG/HOS cells were seeded into a 24 well plate and incubated at 37 °C for 12 h. Then, the original culture was replaced with 500 μL of fresh medium containing Ce6-labeled nanocomposites and further incubation at 37 °C for 4 h. For competitive inhibition experiments, the cells were pretreated with serum-free medium containing free FA for 2 h and then incubated with mFe_3O_4@PDA-FA/Ce6 NPs (mFe@PDA-FA/Ce6 NPs) for 2 h. After that, the cells were gently rinsed with PBS three times to remove excess nanocomposites, followed by incubation with Hoechst 33342 (10 μg mL^{-1}) for 20 min. Finally, the cells were washed twice with PBS and fluorescence imaging of the cells was performed by inverted fluorescence microscope.

Live-Dead Staining Experiments

The calcein AM/PI dual-color fluorescence staining was conducted to evaluate the synergistic killing effect. In brief, MNNG/HOS cells were seeded in 24 well plate at a density of 5×10^4 cells per well and cultured overnight. The cells were divided into 4 groups: (1) control, (2) mFe_3O_4, (3) mFeB@PDA-FA, (4) mFeB@PDA-FA + NIR. After complete adherence, the old medium was replaced with fresh medium containing aforementioned formulations and cultured for 24 h. Finally, the cells were stained with calcein-AM (2 μM) and PI (2 μM) for 10 min, followed by washing with PBS twice and imaged by a fluorescence microscopy.

Detection of Intracellular ˙OH Generation

The intracellular ˙OH production was detected by fluorescence change of DCFH-DA. Briefly, MNNG/HOS cells were seeded in a 6-well plate (1×10^5 cells per well) and incubated at 37 °C in a humidified atmosphere of 5% CO_2 for 24 h. After removing the old medium, fresh medium containing different formulations were added according to the following groups: (1) control, (2) mFe_3O_4, (3) mFeB@PDA-FA, (4) mFeB@PDA-FA + NIR. After incubation for another 6 h, the old medium was replaced with fresh medium again, and the illumination group was irradiated with 808 nm laser (1 W cm^{-2}) for 5 min. Then, the cells were gently rinsed with PBS and incubated with DCFH-DA (10 mM) for 30 min. Finally, the intracellular ˙OH generation was evaluated by an inverted fluorescence microscope.

Mitochondrial Membrane Potential Detection

The changes of mitochondrial membrane potential were measured by JC-1 staining. In brief, MNNG/HOS cells were seeded into a 24-well plate at a density of 5×10^4 cells per well and cultured at 5% CO_2 at 37 °C for 12 h. Afterwards, according to the above grouping, the cells were incubated with serum-free medium containing different formulations for 6 h, followed by irradiating with 808 nm laser (1 W cm^{-2}) for 5 min in the illumination group. Then, the cells were stained with 1 mL of JC-1 solution (10 μg mL^{-1}) for 30 min in dark. After washing three times with PBS, the cells were incubated with DAPI for 10 min and the fluorescence intensity of monomers and aggregates was observed using fluorescence microscopy.

Hemolysis Assay

The fresh blood samples were collected from healthy BALB/c nude mice through heart puncture. Then, the blood samples were centrifuged at 3000 rpm and 4 °C for 5 min to obtain red blood cells (RBCs), which were subsequently washed three times with PBS and diluted in PBS at a ratio of 1:10. Subsequently, 100 μL of RBCs suspension was mixed

with 900 μL of DI water (positive control), PBS (negative control), and mFeB@PDA-FA PBS suspensions with various concentrations (25–800 μg mL^{-1}). After incubation at 37 °C for 2 h, the upper supernatant was obtained by centrifugation at 3000 rpm for 5 min and the absorbance was measured at 570 nm using a microplate reader.

In vivo Imaging

The tumor-bearing mouse model was established by subcutaneous injection of 200 μL MNNG/HOS cells (1×10^7 cells mL^{-1}) into the right flank of 4-week-old BALB/c nude mouse. When the tumor volume reached ~ 100 mm^3, Ce6-labeled nanocomposites were injected into the tumor-bearing mice through the tail vein, and then the fluorescence images were captured using the IVIS system (PerkinElmer, Caliper Life Sciences, MA, USA) at specific time points (0, 1, 3, 6, 12, 24 h). Subsequently, after 24 h of injection, the mice were sacrificed and the major organs (heart, liver, spleen, lung, kidney) and tumor tissues were harvested for ex vitro fluorescence imaging and fluorescence semi-quantitative statistical analysis.

In vivo Photothermal Performance and Antitumor Efficacy

Female BALB/c nude mice (4 weeks old) were purchased from HFK Bioscience Co., LTD and maintained under pathogen-free conditions. All of the experimental procedures were performed in accordance with the Institutional Animal Care and Use Committee guidelines approved by the Animal Laboratory Center of the Fourth Hospital of Hebei Medical University (W2023001). The MNNG/HOS tumor-bearing mice were randomly divided into four groups (n = 5) and received the following treatments: (1) control, (2) mFe_3O_4, (3) mFeB@PDA-FA, (4) mFeB@PDA-FA + NIR. According to the treatment regimen, 200 μL of PBS, mFe_3O_4 solution, and mFeB@PDA-FA solution were injected into the mice every four days through the tail vein. At 6 h after intravenous administration, the tumor-bearing mice in the group (4) received 808 nm laser irradiation at a power density of 1.0 W cm^{-2} for 5 min. The tumor volumes and body weights for each mouse were recorded every other day during the 14-day treatment period. At the end of the treatment, all mice were sacrificed and the major organs (heart, liver, spleen, lung, kidney) were collected for hematoxylin and eosin (H&E) staining to evaluate the biosafety of the nanocomposites. Furthermore, H&E staining, Ki-67 and GPX4 immunofluorescence staining were performed on tumor sections in each group to evaluate the performance of synergistic therapy.

Statistical Analysis

Each experiment was repeated at least three times in parallel and the experimental results were presented as mean ± standard deviation (SD). Student's *t*-test and one-way analysis of variance were used to analyze the significant differences of the results, where $*p < 0.05$, $**p < 0.01$, $***p < 0.001$ were considered statistically significant differences.

Results and Discussion

Preparation and Characterization of mFeB@PDA-FA NPs

In this study, a multifunctional nanomedicine system was developed to effectively amplify the intratumor oxidative stress by combining the inhibition of GSH biosynthesis with photothermal-enhanced CDT therapeutic strategy. The fabrication process of mFeB@PDA-FA is shown in Figure 1A. First, monodisperse Fe_3O_4 NPs with mesoporous structure were fabricated and the size and morphology of mFe_3O_4 NPs were explored by transmission electron microscopy (TEM) and scanning electron microscopy (SEM). As shown in Figure 1B and Figure S1, the SEM and TEM images revealed that the synthesised mFe_3O_4 NPs were approximately spherical in shape and uniform in size with an average diameter of ~ 165 nm. Furthermore, the clearly visible ordered mesoporous structure of the NPs was also observed in the TEM image, indicating that mFe_3O_4 NPs could serve as an excellent nano-vehicle for the encapsulation of BSO molecules. This observation was also confirmed by the N_2 adsorption-desorption analysis of mFe_3O_4, from which the BET surface area and pore size were determined to be 37.81 m^2 g^{-1} and 11.84 nm, respectively (Figure 1D and E). The crystal structure of mFe_3O_4 was investigated by the X-ray diffraction (XRD) analysis. As shown in Figure S2, the characteristic X-ray diffraction peaks of mFe_3O_4 NPs matched well with the standard peak of magnetite (JCPDS 97-002-7899), indicating the successful preparation of mFe_3O_4 NPs. Furthermore, the X-ray photoelectron spectroscopy (XPS) was performed to

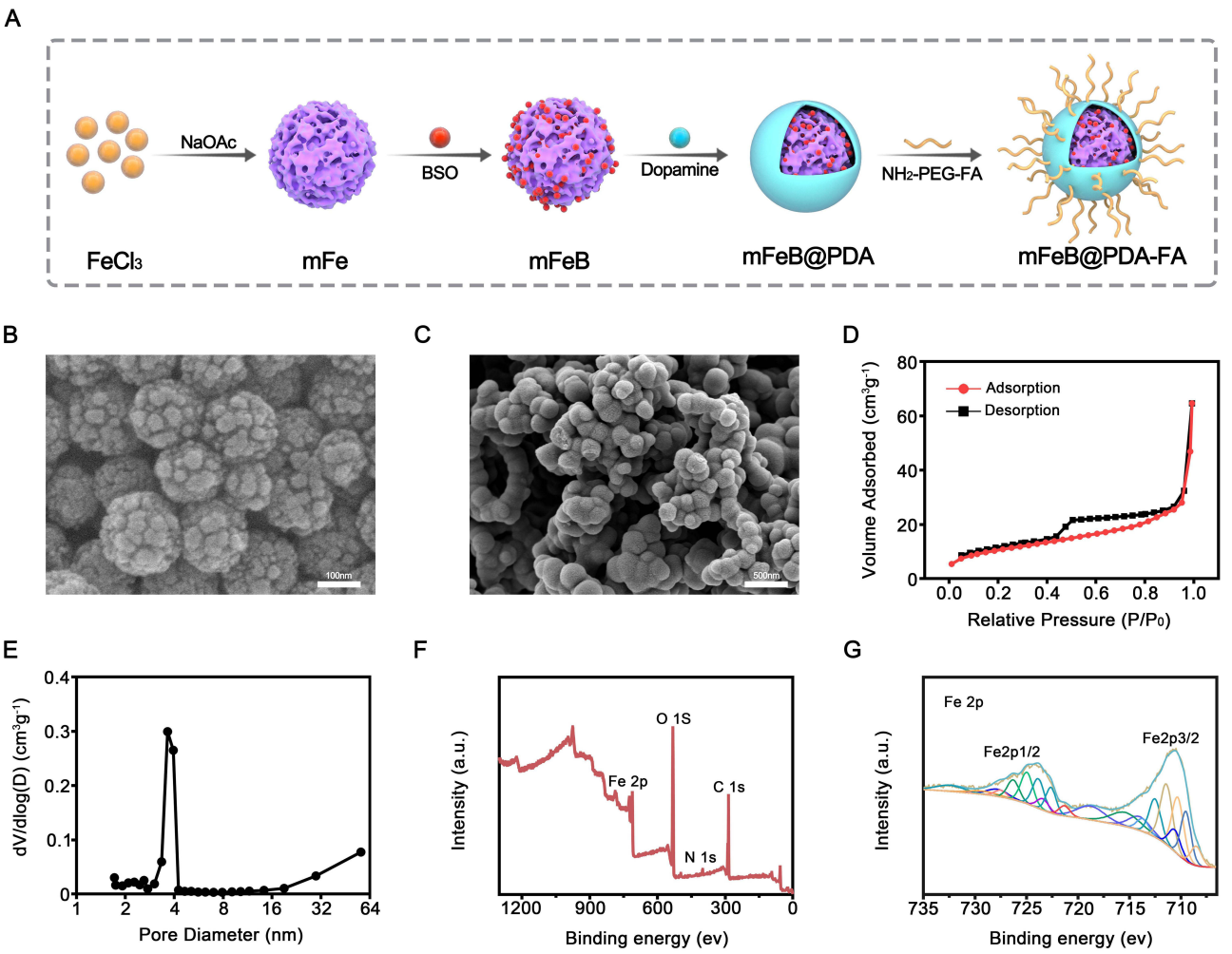

Figure 1 (**A**) Schematic overview of the preparation process of mFeB@PDA-FA NPs. SEM images of (**B**) mFe NPs and (**C**) mFeB@PDA-FA NPs. (**D**) N_2 adsorption-desorption isotherm and (**E**) the corresponding Barrett-Joyner-Halenda (BJH) pore size distribution of mFe NPs. (**F**) XPS survey spectra of mFe NPs. (**G**) Fe 2p XPS spectra of mFe NPs.

investigate the elemental composition of mFe_3O_4 as well as the mixed valence of Fe. As shown in Figure 1F and Figure S3, the fully scanned XPS spectra exhibited distinct spectra for C (1s), O (1s) and Fe (2p) at 284.64, 531.27 and 710.38 ev, respectively. In the high-resolution XPS spectrum of Fe (2p), the peaks located at 709.5 and 722.6 ev could be attributed to the the $2p_{3/2}$ and $2p_{1/2}$ split orbitals of Fe^{2+} ions, while the peaks located at 711.4 and 725 eV could be attributed to the the $2p_{3/2}$ and $2p_{1/2}$ split orbitals of Fe^{3+} ions (Figure 1G). After the drug loading, in order to avoid unnecessary leakage of drugs under physiological circulation conditions and endow the nanotherapeutic platform with ideal tumor targeting ability, the drug-loading NPs were immersed in a dopamine Tris solution and a PDA shell was wrapped on the surface of the nanoparticles by the self-polymerization of dopamine under alkaline conditions, followed by folic acid modification (Figure 1C and Figure S4). The loading and encapsulation rate of BSO were determined by high performance liquid chromatography (HPLC) to be 8.2% and 23.7%, respectively. Meanwhile, the results of precise elemental mapping exhibited the homogeneous distribution of Fe, O, C, N and S in the mFeB@PDA-FA NPs, which further confirmed the successful loading of the drug and the coating of PDA (Figure S5). The dynamic light scattering (DLS) results showed that the hydrodynamic diameter of mFeB@PDA-FA was larger than that of mFe_3O_4 NPs, which is consistent with the SEM results (Figure S6). Moreover, the coating process was monitored by determining the zeta potential of nanoparticles during preparation. As shown in Figure S7, the negative zeta potential was mainly due to the presence of carboxyl groups on the surface of mFe_3O_4 NPs. After coating the PDA shell, the zeta potential changed from -30.27 ± 2.03 mv to -18.07 ± 1.27 mv for the existence of catechol groups on the surface of mFeB@PDA. After folic

acid grafting, the zeta potential of mFeB@PDA-FA eventually stabilized at about −15.57 mv, which not only allowed it steadily dispersible in aqueous solution but also effectively avoided the scavenging effect of phagocytes and prolonged blood circulation in vivo, thus effectively accumulating into tumor tissues. In addition, after the coupling of mFeB@PDA NPs with FA-PEG-NH_2, a characteristic vibration peak of C-O-C was observed at 1112 cm^{-1} in the Fourier transform infrared (FTIR) spectra of mFeB@PDA-FA, which is specific to FA-PEG-NH_2, confirming the successful grafting of FA molecules (Figure S8).[37] More importantly, the constructed nanoparticles could form stable suspensions under various physiological conditions. After 5 days of incubation with PBS and serum, the particle size and the zeta potential of mFeB@PDA-FA exhibited no significant change, indicating excellent stability for long blood circulation (Figure S9).

In vitro Photothermal Performance

The photothermal conversion performance of the synthesized mFeB@PDA-FA NPs was evaluated using a NIR laser with a wavelength of 808 nm and the real-time temperature changes of different preparations were recorded by an IR thermal imaging camera. As shown in Figure 2A, the temperature of both mFe and mFe-based nanocomposites exhibited a significant elevation compared to DI water. Furthermore, the encapsulation of the PDA enhanced the photothermal responsiveness of the nanocomposites, which could be attributed to the ideal photothermal conversion property of the PDA shell. As expected, the η value of mFeB@PDA-FA was calculated to be 49.1% (Figure 2D and E) at 808 nm, which

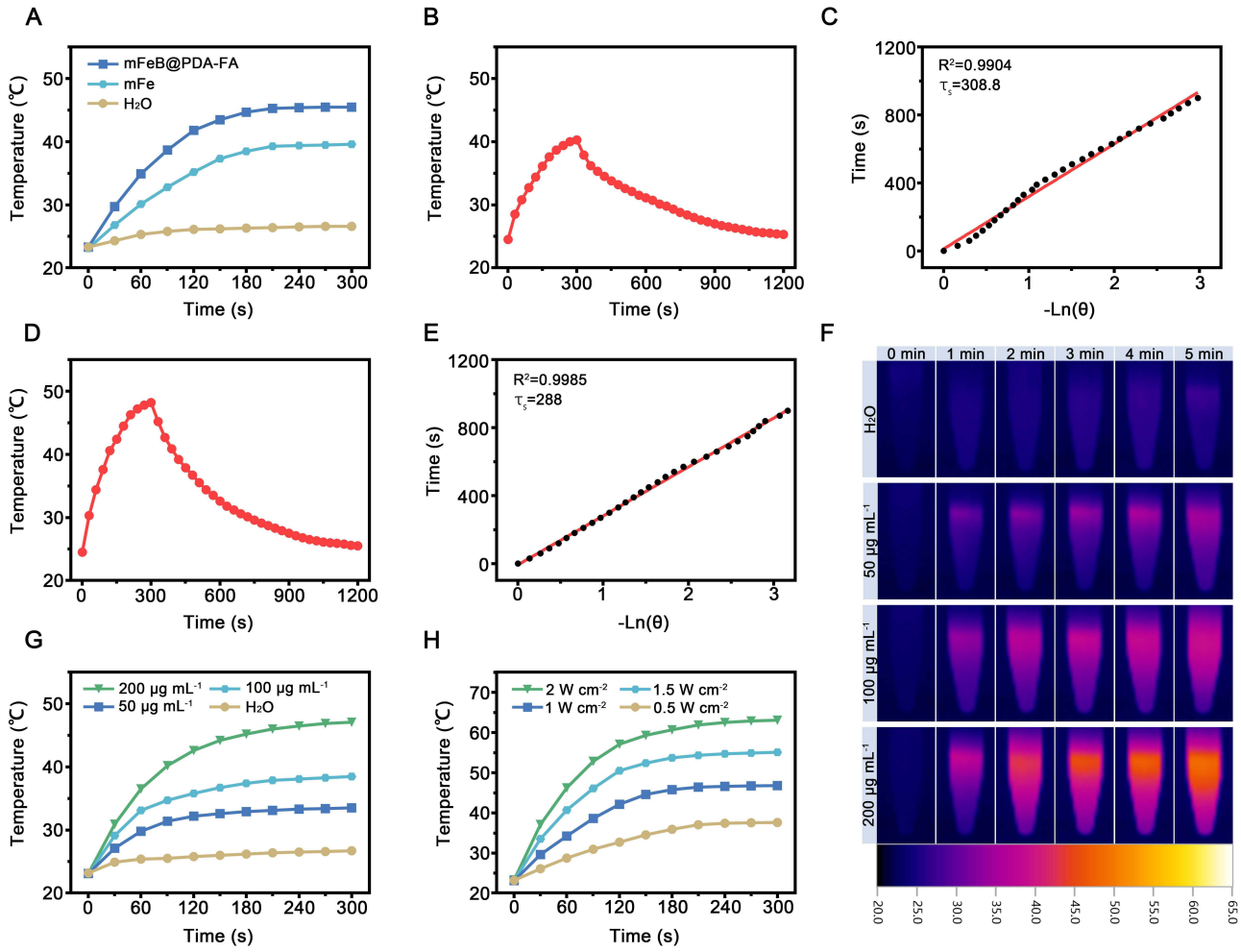

Figure 2 (**A**) Temperature elevation curves of DI water, mFe NPs and mFeB@PDA-FA NPs under 808 nm laser (1.0 W cm^{-2}) irradiation for 5 min. The heating and cooling curves of (**B**) mFeB suspension and (**D**) mFeB@PDA-FA suspension under 808 nm laser irradiation. The liner relationship between -lnθ and time of (**C**) mFeB suspension and (**E**) mFeB@PDA-FA suspension in the cooling stage. (**F**) Infrared thermal images corresponding to different concentrations of mFeB@PDA-FA solution under 808 nm laser (1.0 W cm^{-2}) irradiation. (**G**) Temperature elevation curves of mFeB@PDA-FA solution with different concentrations under 808 nm laser (1.0 W cm^{-2}) irradiation. (**H**) Temperature elevation curves of mFeB@PDA-FA solution for different laser power densities.

was higher than that of mFe_3O_4 suspensions (Figure 2B and C). Moreover, mFeB@PDA-FA NPs exhibited obvious concentration-dependent photothermal conversion properties under 808 nm laser (1W cm^{-2}, 5 min) irradiation. As shown in Figure 2F and G, compared with the negligible temperature increase in the DI water group, the temperature of the mFeB@PDA-FA suspension with a series of concentration gradients showed a significant concentration- and time-dependent elevation after 5 min of 808 nm laser irradiation. Meanwhile, the NIR induced thermal effect of mFeB@PDA-FA was further investigated under 808 nm laser irradiation with different power densities (0.5, 1.0, 1.5, 2.0 W cm^{-2}), which exhibited a strong laser power-dependent photothermal heating effect for mFeB@PDA-FA NPs with a maximum temperature elevation of up to 63.1 °C (Figure 2H). More importantly, given that the nanocomposites may be subjected to multiple photoheating processes throughout the entire treatment process, the photothermal stability of mFeB@PDA-FA NPs was detected by recording the temperature changes during 5 cycles of ON/OFF irradiation. As shown in Figure S10, no discernible temperature decay or obvious change in the temperature variation curves was observed after 5 successive cycles of irradiation. Based on the above results, it is reasonable to believe that mFeB@PDA-FA NPs with excellent photothermal conversion performance and photothermal stability is an ideal photothermal agent for biological PTT.

After confirming the excellent photothermal properties of mFeB@PDA-FA NPs, the release of Fe ions in vitro under different pH values and 808 nm laser irradiation conditions was further investigated. As shown in Figure S11, the release of $Fe^{2/3+}$ ions from mFeB@PDA-FA NPs exhibits a slow release profile at pH level of 7.4, with only 0.82% of the $Fe^{2/3+}$ ions being released within 24 h. In contrast, the amount of $Fe^{2/3+}$ ions released from mFeB@PDA-FA NPs at pH 6.0 was significantly higher than that of pH 7.4, reaching 2.54% within 24 h. This phenomenon can be attributed to the acid-responsive depolymerization of the PDA shell and mFe_3O_4 NPs are more easily decomposed into $Fe^{2/3+}$ ions in an acidic environment. This result further confirmed the specific response of the mFeB@PDA-FA NPs to the slightly acidic tumor environment. More importantly, the release behavior of $Fe^{2/3+}$ ions can be further enhanced under 808 nm laser irradiation, thereby enabling the release of more $Fe^{2/3+}$ ions in the tumor microenvironment to trigger the Fenton reaction to kill tumor cells.

Biocompatibility Evaluation of mFeB@PDA-FA NPs

Good biocompatibility is one of the important prerequisites for the application of nanocomposites in vivo. Therefore, a hemolysis assay was performed to assess the hemocompatibility of mFeB@PDA-FA. As shown in Figure S12, a significant hemolysis was observed in DI water, whereas the RBCs incubated with various concentrations of nanocomposites did not show obvious damage with the hemolysis rate less than 5% even at the highest concentration (800 μg mL^{-1}). Furthermore, the cytotoxicity of mFeB@PDA-FA was evaluated in bone marrow stromal cells (BMSCs) and human umbilical vein endothelial cell line cells (HUVECs) by CCK8 assay. As shown in Figure S13, there was no significant decrease in the survival rates of HUVECs and BMSCs after incubation with different concentrations of mFeB@PDA-FA for 24 or 48 h. These results confirmed that mFeB@PDA-FA with desirable hemocompatibility and excellent biocompatibility could be used as a nanotherapeutic platform for systemic intravenous administration.

Evaluation of Chemodynamic Performance

The Fenton reaction follows a quasi-first-order kinetic model, accompanied by a certain activation energy barrier. The increase of temperature can boost the energy of reactant molecules and promote the effective collision, thereby accelerating the reaction rate and resulting in an increased amount of ˙OH generated per unit time. In order to explore the promotion effect of hyperthermia on the catalytic performance of nanocomposites, the ability of mFe_3O_4 to catalyze H_2O_2 to produce ˙OH at different temperatures was further investigated. Electron spin resonance (ESR) spectroscopy could be regarded as a convincing means to identify ˙OH generation by using 5.5-dimethyl-1-pyrroline N-oxide (DMPO) as the probe to capture the short-lived ˙OH. As shown in Figure 3B, considerable levels of ˙OH were produced in mFe_3O_4 + H_2O_2 group under mildly acidic and hyperthermia conditions as demonstrated by the characteristic 1:2:2:1·˙OH signal in the ESR spectrum. These results revealed that the local high temperature could accelerate the Fenton reaction of Fe ions to produce a large amount of ˙OH in the tumor mildly acidic microenvironment.

Considering the effect of thermal enhancement on promoting ˙OH generation, the catalytic activity of mFe_3O_4 was further evaluated by a colorimetric reaction based on 3,3,5,5-tetramethyl-benzidine (TMB). The peroxidase-like activity of Fe ions

could disintegrate H_2O_2 into ˙OH, which could oxidize TMB to blue-colored oxTMB, accompanied by an increase in the characteristic absorbance at 652 nm (Figure 3A). The temperature of the reaction system with or without 808 nm laser irradiation was simulated by a water bath with different temperatures (25 °C, 45 °C). As shown in Figure S14, there was no obvious absorbance changes in the pure PBS and PBS + H_2O_2 group, while characteristic absorption peak at 652 nm was observed in the mixed solution containing mFe_3O_4 NPs, TMB and H_2O_2. As expected, the absorbance of the reaction system at 652 nm was further increased at higher temperature, indicating the positive promoting effect of hyperthermia on Fe^{2+}-dependent peroxidase-like activity.

In order to further clarify the catalytic performance of mFe_3O_4 NPs, the typical Michaelis-Menten steady-state kinetics of the reactions between mFe_3O_4 and H_2O_2 was determined using biue-colored oxTMB as an indicator of ˙OH generation. Initially, the time-dependent absorbance curves were obtained by adding H_2O_2 to mFe_3O_4 suspension with a fixed concentration at different temperatures (Figure 3C and F). The initial reaction rate (v_0) corresponding to different H_2O_2 concentrations was calculated using the Beer-Lambert law (Eq (2)) according to the change of absorbance at 652 nm in a specified time period. Subsequently, the scatter diagram was plotted with various concentrations of H_2O_2 as the abscissa and the corresponding v_0 as the ordinate, followed by fitting with the Michaelis-Menten curve (Eq (3) and Figure 3D). Furthermore, the K_m and V_{max} of the catalytic reaction at room temperature were calculated to be 18.76 mM and 2.86×10^{-8} M s^{-1}, respectively by Lineweaver-Burk plot (Eq (4) and Figure 3E). In addition, considering the promotion effect of local high temperature on

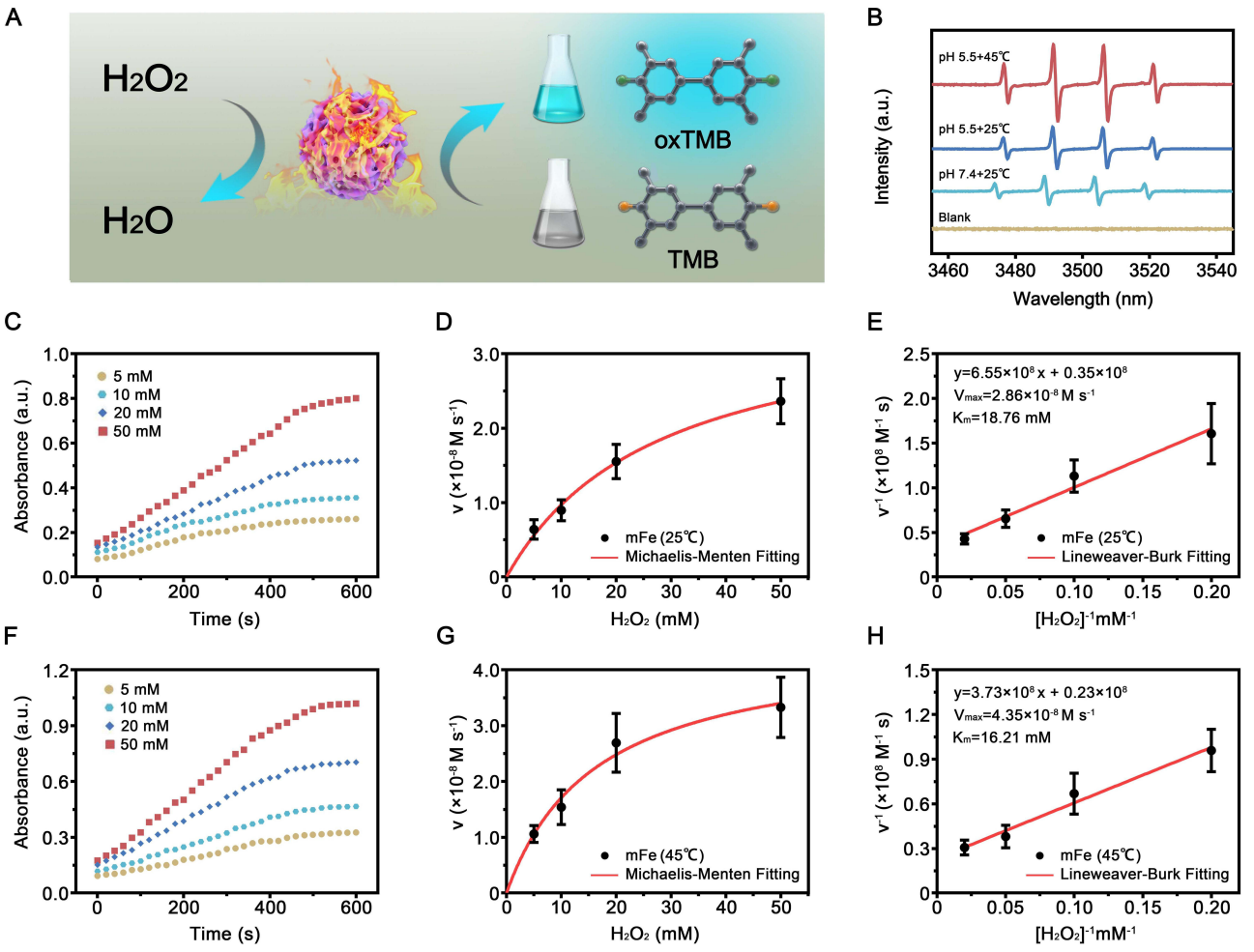

Figure 3 (**A**) Schematic illustration of colorimetric reaction induced by the catalysis of mFe NPs. (**B**) ESR spectra of different reaction systems using DMPO as the spin trap. (**C** and **F**) Time-course absorbance changes at 652 nm as a result of the catalyzed oxidation of TMB at (**C**) 25 °C and (**F**) 45 °C with the addition of elevated concentrations of H_2O_2. (**D, E, G** and **H**) Michaelis-Menten kinetics and Lineweaver-Burk plotting of mFe NPs with elevated concentrations of H_2O_2 as the substrate at (**D** and **E**) 25 °C and (**G** and **H**) 45 °C.

peroxidase-like activity, the catalytic performance of mFe_3O_4 was further investigated by TMB-induced colorimetric reaction at 45 °C with different concentrations of H_2O_2 as substrate. As expected, the catalytic reaction at high temperature also followed the Michaelis-Menten behavior and the K_m and V_{max} were determined to be 16.21 mM and 4.35×10^{-8} M s^{-1}, respectively, according to aforementioned procedure (Figure 3G and H). Compared with V_{max} at room temperature, the elevated V_{max} promoted by the hyperthermia demonstrated that PTT could achieve more ideal anti-tumor efficacy by facilitating the Fenton reaction.

Cellular Uptake Assay

The effective endocytosis of nanocomposites by tumor cells is one of the prerequisites for the realization of tumor synergistic therapy.[38] Thanks to the red fluorescence of Ce6, the cellular uptake behavior of free Ce6 or Ce6-labeled nanocomposites by MNNG/HOS cells was investigated by a fluorescence microscopy. As shown in Figure 4A, after incubation of free Ce6 with MNNG/HOS cells for 4 h, only weak red fluorescence signal was observed, indicating that Ce6 was not effectively taken up by tumor cells due to its poor solubility. In contrast, the fluorescence intensity in mFe@PDA/Ce6 group was stronger than that in the free Ce6 group, which could be attributed to the improvement of cell uptake behavior due to the presence of PDA shell. More importantly, due to the overexpression of folate receptor on

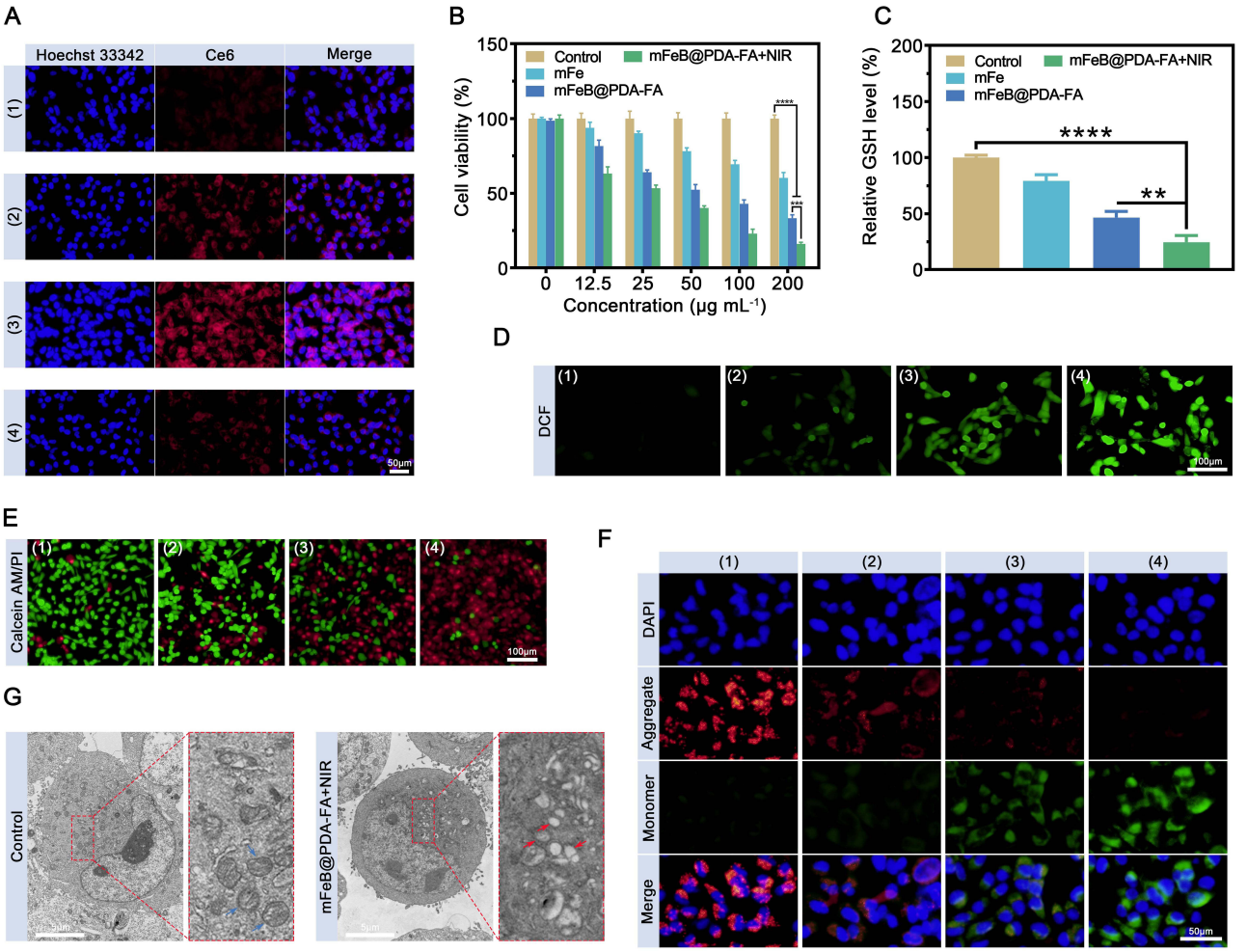

Figure 4 (**A**) Fluorescence microscopy images of MNNG/HOS cells after incubation with (1) free Ce6, (2) mFe@PDA/Ce6, (3) mFe@PDA-FA/Ce6, (4) mFe@PDA-FA/Ce6 + free FA. (**B**) The cell viability of MNNG/HOS cells after co-incubation with mFe, mFeB@PDA-FA and mFeB@PDA-FA + NIR. (**C**) Intracellular GSH level of MNNG/HOS cells after treated with mFe, mFeB@PDA-FA and mFeB@PDA-FA + NIR. (**D**) DCFH-DA staining, (**E**) calcein-AM/PI double staining and (**F**) JC-1 staining of MNNG/HOS cells after different treatments: (1) control, (2) mFe, (3) mFeB@PDA-FA, (4) mFeB@PDA-FA + NIR. (**G**) Bio-TEM images of micromorphological changes of MNNG/HOS cells after different treatments. The blue and red arrows indicate relative normal and damaged mitochondria, respectively.

various tumor cells surface, the FA modification significantly increased the uptake efficiency of MNNG/HOS cells for mFe@PDA-FA/Ce6, which could be confirmed by the brightest red fluorescence in the mFe@PDA-FA/Ce6 group. In addition, a competitive inhibition assay of FA molecule was further conducted to explore the targeting ability of FA. As expected, pretreatment with free FA molecules significantly reduced the fluorescence intensity of MNNG/HOS cells compared to the stronger fluorescence signal in mFe@PDA-FA/Ce6 group, demonstrating that FA is one of the critical factors in mediating cell endocytosis.

In vitro GSH Elimination and Synergistic Cytotoxicity

The in vitro cytotoxicity of different formulations on MNNG/HOS cells was evaluated by the typical CCK-8 assay. As shown in Figure 4B, mFe_3O_4-based nanocomposites exhibited obvious dose-dependent cytotoxicity. Among all treatment groups, the mFeB@PDA-FA group exhibited remarkable tumor inhibition efficiency after irradiation with 808 nm laser (1 W cm^{-2}) for 5 min, with a inhibition rate up to 83.7% at a concentration of 200 μg mL^{-1}. These results could be attributed to the synergistic enhancement of PTT-induced hyperthermia on ferroptosis.

The fabricated synergistic nanotherapeutic platform mFeB@PDA-FA was designed to elevate intratumor oxidative stress level by promoting ROS generation and inhibiting GSH biosynthesis. Given that BSO-blocked GSH replenishment is a critical factor in ROS accumulation, the intracellular GSH level of different groups were detected by a GSH and GSSD assay kit. As shown in Figure 4C, after co-incubation with BSO-containing nanocomposites, the intracellular GSH level in MNNG/HOS cells showed a significant decrease compared to the control group, and with the intervention of 808 nm laser irradiation, the GSH content in mFeB@PDA-FA + NIR group showed a further decline. These results suggested that the increased endocytosis of nanocomposites and hyperthermia-enhanced nanocatalytic therapy could significantly reduce the intracellular GSH level. More importantly, the consumption of GSH can lead to the inactivation of GPX4, which deprives GPX4 of its ability to catalyze lipid peroxides reduction. Therefore, the GPX4 activity in different groups was evaluated by monitoring the decrease in absorbance of nicotinamide adenine dinucleotide phosphate (NADPH) at 340 nm. As shown in Figure S15, the GPX4 activity decreased significantly in the mFeB@PDA + NIR group, which was confirmed by the change of NADPH content over time.

Excessive production and accumulation of ROS could lead to intracellular redox imbalance and ferroptosis.[39] Therefore, the intracellular ROS content in different groups were detected by a ROS-sensitive probe DCFH-DA, which could be oxidized by ROS to produce 2.7-dichlorofluorescein (DCF) with green fluorescence.[40] As shown in Figure 4D, compared with the negligible green fluorescence in the control group, there was an obvious green fluorescence signal in the mFeB@PDA-FA group, which intensity could be further enhanced after 808 nm laser irradiation.

Furthermore, encouraged by the aforementioned GSH elimination and effective ROS accumulation, the effect of this combination therapy on LPO performance was further evaluated in vitro. The lipid peroxidation sensor C11-$BODIPY^{581/591}$ was used to evaluate the lipid peroxide levels after different treatments. As shown in Figure S16, the cells of mFeB@PDA-FA + NIR group showed stronger fluorescence intensity than those of other groups, which indicated the effectiveness of mFeB@PDA-FA in inducing LPO. In addition, the typical LPO process involves ROS attacking unsaturated lipids to form lipid radicals, followed by the production of lipid peroxy radical in the presence of oxygen. Finally, lipid peroxides breaks down into small molecular by-products, in which malondialdehyde (MDA) fragments are considered to be one of the main end products (Figure S17).[41,42] As shown in Figure S18, the MDA content in the mFeB@PDA-FA + NIR treatment group increased significantly compared with the other three groups, indicating that the combination of GSH elimination and photothermal-enhanced ROS generation could promote the occurrence of LPO for activating ferroptosis.

Ferroptosis refers to a form of cell death that relies on iron and LPO, which is mainly characterized by iron accumulation and increased lipid peroxides, resulting in the destruction of cell membrane structure and cell death. The combination of hyperthermia-enhanced Fenton reaction and GSH inhibition can accelerate the ·OH oxidation of intracellular liposomes, thus causing irreversible damage to cells and significantly enhancing ferroptosis. Therefore, in order to more intuitively exhibit the killing effect of synergistic nanocatalytic therapy on tumor cells, Calcein-AM/PI staining was performed on MNNG/HOS cells after different treatments. As shown in Figure 4E, compared with the large area of green fluorescence in the control group, a gradual decrease in the green fluorescence region and a gradual increase

in the red fluorescence region were observed in the three subsequent treatment groups, demonstrating the powerful tumor killing effect of this synergistic therapy. Moreover, the close relationship between mitochondrial dysfunction and cell apoptosis has been confirmed by many studies.[43] The depolarization of mitochondrial membrane potential of MNNG/HOS cells after different treatments was monitored by a JC-1 fluorescent probe, which could emit red fluorescence in the form of aggregates in the normal mitochondrial matrix while emit green fluorescence in the form of monomer in the unhealthy mitochondria.[44,45] As shown in Figure 4F, a bright red fluorescence signal of the JC-1 aggregates was observed in the control group, which intensity gradually decreased in the subsequent treatment, accompanied by the gradual enhancement of green fluorescence of JC-1 monomer, These results indicated that the treatment of mFeB@PDA-FA + NIR could lead to the reduction of mitochondrial membrane potential of MNNG/HOS cells. Further, the morphological changes of mitochondria after different treatments were observed by bio-TEM. As indicated, the mitochondrial morphology in mFeB@PDA-FA + NIR group showed dramatic changes, including volume reduction, increased membrane density and mitochondrial ridges destruction (Figure 4G). Collectively, all the results indicated that mFeB@PDA-FA could effectively disrupt redox homeostasis through PTT-enhanced Fenton reaction and BSO-blocked GSH biosynthesis, thus achieving desirable tumor killing effect.

In vivo Biodistribution and Photothermal Performance

The specific tumor targeting of nanocomposites is one of the prerequisites for their synergistic treatment of tumors.[46] Therefore, the biodistribution of nanocomposites in MNNG/HOS tumor-bearing mice was investigated by in vivo fluorescence imaging. As shown in Figure 5A, the fluorescence signal of the tumor region gradually increased with time and reached a plateau at 6 h post-injection, which provided a basis for us to select the optimal illumination time. Interestingly, residual fluorescence signal was still detectable in the tumor region 24 h after intravenous injection, indicating that the nanocomposites were able to achieve a high degree of retention within the tumor. At 24 h after intravenous injection, the mice were sacrificed and tumor tissues and major organs (heart, liver, spleen, lung, kidney) were collected for ex vivo fluorescence imaging (Figure 5B). The results of semiquantitative mean fluorescence intensity

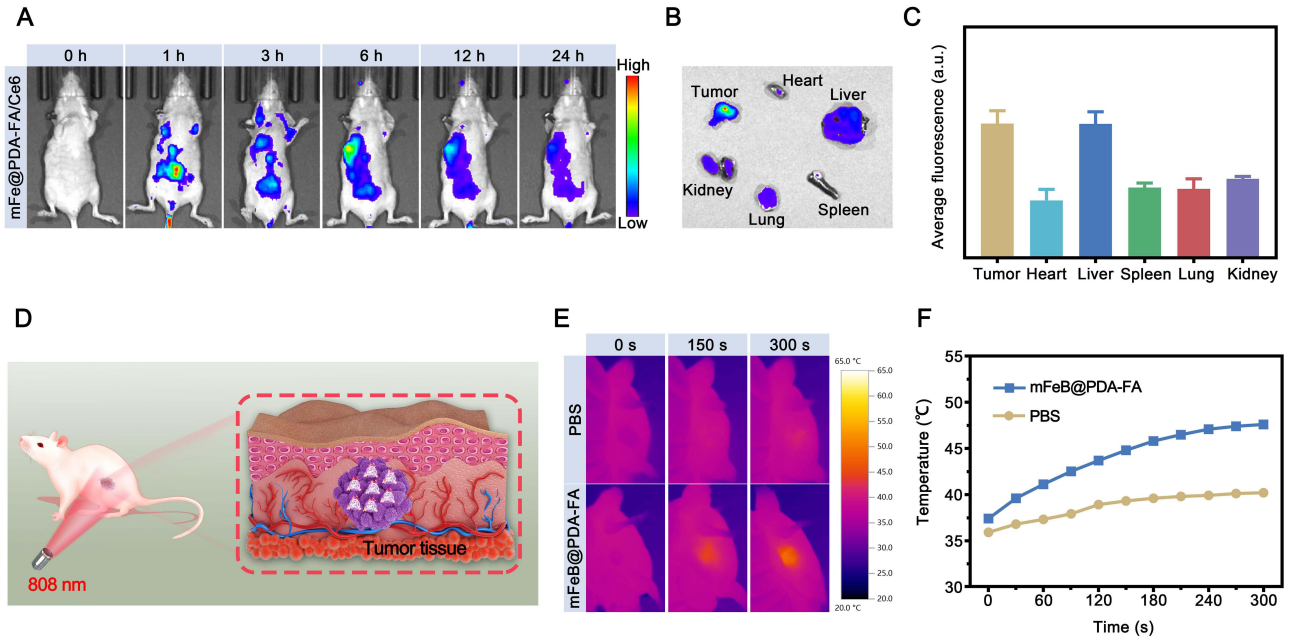

Figure 5 (**A**) Fluorescence distribution images of MNNG/HOS tumor-bearing mice intravenously injected with mFe@PDA-FA/Ce6 at different time points. (**B**) Ex vivo fluorescence images of major organs (heart, liver, spleen, lung and kidney). (**C**) Fluorescence semiquantitative analysis of tumor tissues and major organs (heart, liver, spleen, lung and kidney). (**D**) Schematic illustration of in vivo photothermal effect of mFeB@PDA-FA NPs under 808 nm laser irradiation. (**E**) Infrared thermal images and (**F**) corresponding temperature elevation curves at the tumor region of MNNG/HOS tumor-bearing mice after intravenous injection of PBS or mFeB@PDA-FA NPs followed by 808 nm laser (1.0 W cm^{-2}) irradiation.

(MFI) analysis showed that the fluorescence signal was mainly concentrated in the tumor and stronger than that in the major organs, which further demonstrated the high tumor uptake and retention ability of the nanocomposites (Figure 5C).

Encouraged by the specific targeted tumor accumulation and ideal photothermal conversion properties of the mFeB@PDA-FA NPs, we further investigated whether mFeB@PDA-FA could achieve desired high temperature at the tumor site to kill tumors after laser irradiation. After 6 h of intravenous injection of mFeB@PDA-FA suspension in tumor-bearing mice, the tumor region was subjected to 808 nm laser irradiation for 5 min and the real-time temperature changes were recorded by an infrared thermal camera (Figure 5D). As shown in Figure 5E and F, the temperature of the tumor region increased slightly in the control group, while the temperature of the mFeB@PDA-FA + NIR group showed a significant increase from 37.4 °C to 47.6 °C within 5 min. This result indicated that mFeB@PDA-FA could accumulate at the tumor site through the EPR effect and the active targeting effect of FA, and then generate hyperthermia under 808 nm laser irradiation by virtue of its excellent photothermal conversion performance to enhance the effect of synergistic therapy.

In vivo Antitumor Efficacy

Encouraged by the excellent therapeutic effects in vitro and favorable photothermal conversion performance of mFeB@PDA-FA in vivo, the synergistic anti-tumor effect of mFeB@PDA-FA in vivo was further explored. As shown in the Figure 6A, MNNG/HOS tumor-bearing mice were randomly divided into four groups (n = 5) and injected with

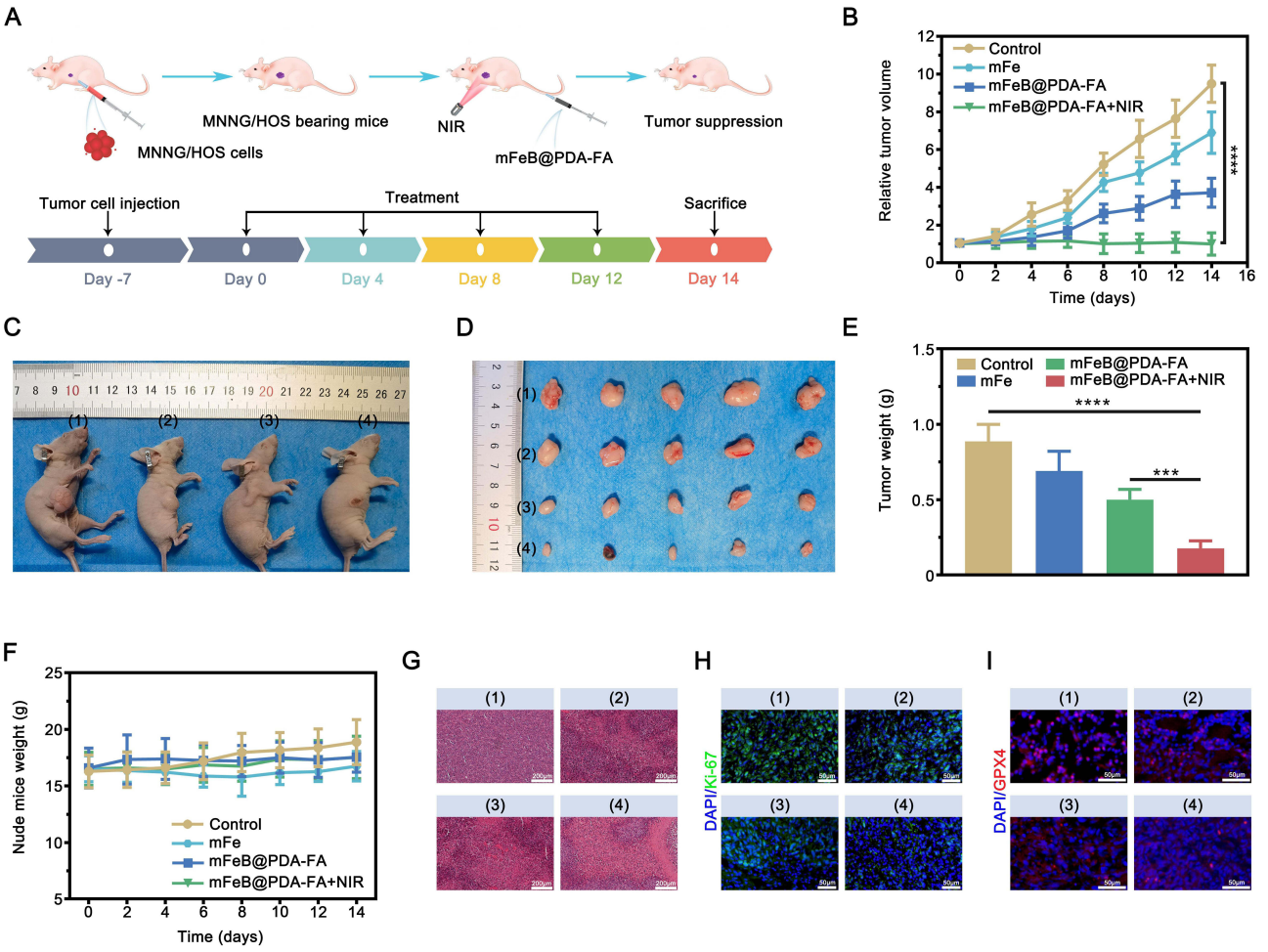

Figure 6 (**A**) Schematic illustration of the creation of MNNG/HOS tumor-bearing mice and the procedures of anticancer treatment. (**B**) Changes in the relative tumor volume of tumor-bearing mice during 14 days-treatment (****P < 0.0001). (**C**) Representative images of tumor-bearing mice and (**D**) digital photographs of tumors after various treatments: (1) control, (2) mFe, (3) mFeB@PDA-FA, (4) mFeB@PDA-FA + NIR. (**E**) Tumor weights in different treatment groups. (**F**) Changes in body weight of tumor-bearing mice during treatment (***P < 0.001, ****P < 0.0001). (**G**) H&E staining, (**H**) Ki-67 immunofluorescence staining and (**I**) GPX4 immunofluorescence staining of tumor tissue sections from different treatment groups: (1) control, (2) mFe, (3) mFeB@PDA-FA, (4) mFeB@PDA-FA + NIR.

corresponding preparations through the tail vein when the tumor grew to an appropriate size: (1) control, (2) mFe_3O_4, (3) mFeB@PDA-FA, (4) mFeB@PDA-FA + NIR. The tumor-bearing mice in group (4) were subjected to 808 nm (1 W cm^{-2}) laser irradiation for 5 min at 6 h post-intravenous injection of mFeB@PDA-FA according to the results of biodistribution in vivo. Throughout the treatment period, the mice received repeated treatment on days 0, 4, 8, 12, respectively, and the tumor volumes and body weights of mice were recorded every other day. As shown in Figure 6B, mFe_3O_4 treatment inhibited tumor growth to a certain extent in mice compared to uncontrolled tumor growth after intravenous administration of PBS, implying that mFe_3O_4 was able to achieve in vivo antitumor efficacy by converting H_2O_2 in the TME into highly toxic $^{\cdot}OH$ through Fe^{2+}-dependent peroxidase-like activity. Unsurprisingly, BSO-blocked GSH biosynthesis and FA-mediated active targeting endowed mFeB@PDA-FA with more desirable anti-tumor effect, which was confirmed by the more pronounced tumor inhibition efficiency in the group (3). More importantly, the best tumor inhibitory effect was achieved by mFeB@PDA-FA + NIR, confirming that photothermal effect could effectively enhance the tumor inhibition effect of the synergistic nanocatalytic therapy in vivo. After 14 days of treatment, the mice were sacrificed and the excised tumors in each group were weighted and photographed. As seen from the visual photographs of tumor-bearing mice and harvested tumors (Figure 6C and D), mFeB@PDA-FA + NIR treatment possessed the most obvious tumor inhibitory effect, which was consistent with the tumor weight results (Figure 6E). In addition, the body weight of the tumor-bearing mice treated with different formulations did not fluctuate obviously throughout the treatment period, indicating that mFeB@PDA-FA possessed good biological safety in vivo and had no significant influence on the growth and development of mice (Figure 6F). Furthermore, H&E staining were performed on tumor slices to investigate the pathological changes of tumor tissues after different treatments. As shown in Figure 6G, a small fraction of necrosis of tumor cells was observed in the mFe_3O_4 treatment group, while the necrotic regions at the tumor sites gradually increased with the progress of nanocatalytic therapy, especially after receiving laser irradiation. Additionally, the cell proliferation in tumor sections was evaluated by Ki-67 immunofluorescence staining. As expected, cell proliferation was significantly inhibited in the mFeB@PDA-FA + NIR treatment group, as evidenced by the lowest Ki-67 antigen expression (Figure 6H). Next, the expression of ferroptosis marker GPX4 in different treatment groups was examined. As shown in Figure 6I, mFeB@PDA-FA + NIR mediated GSH elimination and oxidative damage amplification could effectively reduce the GPX4 level in tumor tissue. These results fully revealed the enhancement effect of photothermal effect on the nanocatalytic therapy. Finally, H&E staining was performed on the major organs (heart, liver, spleen, lung, kidney) of all treatment groups and no significant histological changes were observed (Figure S19). Meanwhile, the blood biochemistry analysis showed no abnormalities in liver function markers (alanine aminotransferase (ALT), aspartate aminotransferase (AST)) and renal function markers (blood urea nitrogen (BUN), creatinine (CREA)) on day 14 after intravenous injection of mFeB@PDA-FA (Figure S20). These results confirmed that mFeB@PDA-FA had a desirable biosafety and deserved to be an ideal candidate for in vivo synergistic tumor therapy.

Conclusions

In summary, a TME-responsive nano-catalytic therapeutic platform (mFeB@PDA-FA NPs) was developed to improve the efficiency of ferroptosis in tumor treatment through photothermal-enhanced Fenton reaction and the inhibition of GSH biosynthesis. This nanotherapeutic platform not only achieved high tumor inhibition efficiency but also provided a new perspective for the subsequent design and development of novel synergistic therapeutic platforms.

Author Contributions

All authors made substantial contributions to the reported work, encompassing conception, study design, execution, data acquisition, analysis and interpretation, or in all these areas. All authors participated in drafting, revising and critically evaluating the article. All authors have granted their final approval for the version intended for publication, concurred on the journal where the article is submitted, and agree to be accountable for all aspects of the work.

Disclosure

The authors declare no conflicts of interest in this work.

References

1. Zhang Y, Song Q, Zhang Y, et al. Iron-Based Nanovehicle Delivering Fin56 for Hyperthermia-Boosted Ferroptosis Therapy Against Osteosarcoma. *Int J Nanomed*. 2024;19. doi:10.2147/IJN.S441112.
2. Mirabello L, Zhu B, Koster R, et al. Frequency of Pathogenic Germline Variants in Cancer-Susceptibility Genes in Patients With Osteosarcoma. *JAMA Oncol*. 2020;6(5):724–734. doi:10.1001/jamaoncol.2020.0197
3. He C, Jiang Y, Guo Y, Wu Z. Amplified Ferroptosis and Apoptosis Facilitated by Differentiation Therapy Efficiently Suppress the Progression of Osteosarcoma. *Small*. 2023;19(44):e2302575. doi:10.1002/smll.202302575
4. Jiang M, Jike Y, Liu K, et al. Exosome-mediated miR-144-3p promotes ferroptosis to inhibit osteosarcoma proliferation, migration, and invasion through regulating ZEB1. *Mol Cancer*. 2023;22(1):113. doi:10.1186/s12943-023-01804-z
5. Chen H, Luo X, Huang QH, et al. Platelet membrane fusion liposome loaded with type I AIE photosensitizer to induce chemoresistance cancer pyroptosis and immunogenic cell death for enhancing cancer immunotherapy. *Chem Eng J*. 2023;476:146276. doi:10.1016/j.cej.2023.146276
6. Zhang N, Ping W, Rao K, et al. Biomimetic copper-doped polypyrrole nanoparticles induce glutamine metabolism inhibition to enhance breast cancer cuproptosis and immunotherapy. *J Control Release*. 2024;371:204–215. doi:10.1016/j.jconrel.2024.05.045
7. Mou Y, Wang J, Wu J, et al. Ferroptosis, a new form of cell death: opportunities and challenges in cancer. *J Hematol Oncol*. 2019;12(1):34. doi:10.1186/s13045-019-0720-y
8. Jiang X, Stockwell BR, Conrad M. Ferroptosis: mechanisms, biology and role in disease. *Nat Rev Mol Cell Biol*. 2021;22(4):266–282. doi:10.1038/s41580-020-00324-8
9. Zhang J, Zhou K, Lin J, et al. Ferroptosis-enhanced chemotherapy for triple-negative breast cancer with magnetic composite nanoparticles. *Biomaterials*. 2023;303:122395. doi:10.1016/j.biomaterials.2023.122395
10. Chen K, Li H, Zhou A, et al. Cell Membrane Camouflaged Metal Oxide-Black Phosphorus Biomimetic Nanocomplex Enhances Photo-chemo-dynamic Ferroptosis. *ACS Appl Mater Interfaces*. 2022;14:26557–26570. doi:10.1021/acsami.2c08413
11. Stockwell BR, Friedmann angeli JP, Bayir H, et al. Ferroptosis: a Regulated Cell Death Nexus Linking Metabolism, Redox Biology, and Disease. *Cell*. 2017;171(2):273–285. doi:10.1016/j.cell.2017.09.021
12. Wang S, Li F, Qiao R, et al. Arginine-Rich Manganese Silicate Nanobubbles as a Ferroptosis-Inducing Agent for Tumor-Targeted Theranostics. *ACS Nano*. 2018;12(12):12380–12392. doi:10.1021/acsnano.8b06399
13. Liu T, Liu W, Zhang M, et al. Ferrous-Supply-Regeneration Nanoengineering for Cancer-Cell-Specific Ferroptosis in Combination with Imaging-Guided Photodynamic Therapy. *ACS Nano*. 2018;12(12):12181–12192. doi:10.1021/acsnano.8b05860
14. Wang Y, Zhou X, Yao L, et al. Capsaicin Enhanced the Efficacy of Photodynamic Therapy Against Osteosarcoma via a Pro-Death Strategy by Inducing Ferroptosis and Alleviating Hypoxia. *Small*. 2024;20:e2306916. doi:10.1002/smll.202306916.
15. Lv -H-H, Zhen C-X, Liu J-Y, Shang P. PEITC triggers multiple forms of cell death by GSH-iron-ROS regulation in K7M2 murine osteosarcoma cells. *Acta Pharmacol Sin*. 2020;41(8):1119–1132. doi:10.1038/s41401-020-0376-8
16. Fu J, Li T, Yang Y, et al. Activatable nanomedicine for overcoming hypoxia-induced resistance to chemotherapy and inhibiting tumor growth by inducing collaborative apoptosis and ferroptosis in solid tumors. *Biomaterials*. 2021;268:120537. doi:10.1016/j.biomaterials.2020.120537
17. Zhou Z, Song J, Tian R, et al. Activatable Singlet Oxygen Generation from Lipid Hydroperoxide Nanoparticles for Cancer Therapy. *Angew Chem Int Ed Engl*. 2017;56(23):6492–6496. doi:10.1002/anie.201701181
18. Jiang Q, Wang K, Zhang X, et al. Platelet Membrane-Camouflaged Magnetic Nanoparticles for Ferroptosis-Enhanced Cancer Immunotherapy. *Small*. 2020;16(22):e2001704. doi:10.1002/smll.202001704
19. Meng Y, Zhang D, Sun Y, et al. Core-shell FePt-cube@covalent organic polymer nanocomposites: a multifunctional nanocatalytic agent for primary and metastatic tumor treatment. *J Mater Chem B*. 2020;8(48):11021–11032. doi:10.1039/d0tb01981j
20. Ursini F, Maiorino M. Lipid peroxidation and ferroptosis: the role of GSH and GPx4. *Free Radic Biol Med*. 2020;152:175–185. doi:10.1016/j.freeradbiomed.2020.02.027
21. Yang WS, SriRamaratnam R, Welsch ME, et al. Regulation of ferroptotic cancer cell death by GPX4. *Cell*. 2014;156(1–2):317–331. doi:10.1016/j.cell.2013.12.010
22. Gao Y, Li Y, Cao H, et al. Hypertoxic self-assembled peptide with dual functions of glutathione depletion and biosynthesis inhibition for selective tumor ferroptosis and pyroptosis. *J Nanobiotechnol*. 2022;20(1):390. doi:10.1186/s12951-022-01604-5
23. Li Z, Guo T, Zhao S, Lin M. The Therapeutic Effects of MUC1-C shRNA@Fe3O4 Magnetic Nanoparticles in Alternating Magnetic Fields on Triple-Negative Breast Cancer. *Int J Nanomed*. 2023;18:5651–5670. doi:10.2147/IJN.S426849
24. Cun J-E, Pan Y, Zhang Z, et al. Photo-enhanced upcycling H2O2 into hydroxyl radicals by IR780-embedded Fe3O4@MIL-100 for intense nanocatalytic tumor therapy. *Biomaterials*. 2022;287:121687. doi:10.1016/j.biomaterials.2022.121687
25. Rao Z, Xia Y, Jia Q, et al. Iron-based metal-organic framework co-loaded with buthionine sulfoximine and oxaliplatin for enhanced cancer chemo-ferrotherapy via sustainable glutathione elimination. *J Nanobiotechnol*. 2023;21(1):265. doi:10.1186/s12951-023-01998-w
26. Chen Z, Liu Z, Zhou Y, et al. Bionic aggregation-induced emission photosensitizer for enhanced cancer immunotherapy. *Mater Today Bio*. 2024;28:101217. doi:10.1016/j.mtbio.2024.101217
27. Wang H, Yang W, Bian K, et al. Oxygen-Deficient BiOCl Combined with L-Buthionine-Sulfoximine Synergistically Suppresses Tumor Growth through Enhanced Singlet Oxygen Generation under Ultrasound Irradiation. *Small*. 2022;18(9):e2104550. doi:10.1002/smll.202104550
28. Yang Z, Qiao C, Jia Q, et al. Redox dyshomeostasis modulation of the tumor intracellular environment through a metabolic intervention strategy for enhanced photodynamic therapy. *Theranostics*. 2022;12(14):6143–6154. doi:10.7150/thno.75837
29. Wang C, Wang J, Pan X, et al. Reversing ferroptosis resistance by MOFs through regulation intracellular redox homeostasis. *Asian J Pharm Sci*. 2023;18(1):100770. doi:10.1016/j.ajps.2022.11.004
30. Ai J-W, Liu B, Liu W-D. Folic acid-tagged titanium dioxide nanoparticles for enhanced anticancer effect in osteosarcoma cells. *Mater Sci Eng C*. 2017;76:1181–1187. doi:10.1016/j.msec.2017.03.027
31. Huang X, Chen J, Wu W, et al. Delivery of MutT homolog 1 inhibitor by functionalized graphene oxide nanoparticles for enhanced chemo-photodynamic therapy triggers cell death in osteosarcoma. *Acta Biomater*. 2020;109:229–243. doi:10.1016/j.actbio.2020.04.009
32. Hu H, Yang W, Liang Z, et al. Amplification of oxidative stress with lycorine and gold-based nanocomposites for synergistic cascade cancer therapy. *J Nanobiotechnol*. 2021;19(1):221. doi:10.1186/s12951-021-00933-1

33. Xuan S, Wang F, Lai JMY, et al. Synthesis of biocompatible, mesoporous Fe(3)O(4) nano/microspheres with large surface area for magnetic resonance imaging and therapeutic applications. *ACS Appl Mater Interfaces*. 2011;3(2):237–244. doi:10.1021/am1012358
34. Zheng R, Wang S, Tian Y, et al. Polydopamine-Coated Magnetic Composite Particles with an Enhanced Photothermal Effect. *ACS Appl Mater Interfaces*. 2015;7(29):15876–15884. doi:10.1021/acsami.5b03201
35. Hu H, Deng X, Song Q, et al. Mitochondria-targeted accumulation of oxygen-irrelevant free radicals for enhanced synergistic low-temperature photothermal and thermodynamic therapy. *J Nanobiotechnol*. 2021;19(1):390. doi:10.1186/s12951-021-01142-6
36. Wu C, Liu Z, Chen Z, et al. A nonferrous ferroptosis-like strategy for antioxidant inhibition-synergized nanocatalytic tumor therapeutics. *Sci Adv*. 2021;7(39):eabj8833. doi:10.1126/sciadv.abj8833
37. Pu X-Q, Ju X-J, Zhang L, et al. Novel Multifunctional Stimuli-Responsive Nanoparticles for Synergetic Chemo-Photothermal Therapy of Tumors. *ACS Appl Mater Interfaces*. 2021;13(24):28802–28817. doi:10.1021/acsami.1c05330
38. Liu H-J, Wang M, Hu X, Shi S, Xu P. Enhanced Photothermal Therapy through the In Situ Activation of a Temperature and Redox Dual-Sensitive Nanoreservoir of Triptolide. *Small*. 2020;16(38):e2003398. doi:10.1002/smll.202003398
39. Wei Y, Wang Z, Yang J, et al. Reactive oxygen species / photothermal therapy dual-triggered biomimetic gold nanocages nanoplatform for combination cancer therapy via ferroptosis and tumor-associated macrophage repolarization mechanism. *J Colloid Interface Sci*. 2022;606(Pt 2):1950–1965. doi:10.1016/j.jcis.2021.09.160
40. Liu X, Geng P, Yu N, et al. Multifunctional Doxorubicin@Hollow-Cu9S8 nanoplatforms for Photothermally-Augmented Chemodynamic-Chemo therapy. *J Colloid Interface Sci*. 2022;615:38–49. doi:10.1016/j.jcis.2022.01.156
41. Hassannia B, Vandenabeele P, Vanden Berghe T. Targeting Ferroptosis to Iron Out Cancer. *Cancer Cell*. 2019;35(6):830–849. doi:10.1016/j.ccell.2019.04.002
42. O'Donnell VB, Aldrovandi M, Murphy RC, Krönke G. Enzymatically oxidized phospholipids assume center stage as essential regulators of innate immunity and cell death. *Sci Signal*. 2019;12(574). doi:10.1126/scisignal.aau2293
43. Zamzami N, Kroemer G. The mitochondrion in apoptosis: how Pandora's box opens. *Nat Rev Mol Cell Biol*. 2001;2(1):67–71. doi:10.1038/35048073
44. Gao J, Wang Z, Guo Q, et al. Mitochondrion-targeted supramolecular "nano-boat" simultaneously inhibiting dual energy metabolism for tumor selective and synergistic chemo-radiotherapy. *Theranostics*. 2022;12(3):1286–1302. doi:10.7150/thno.67543
45. Zhang Y, Qi G, Qu X, Wang B, Ma K, Jin Y. Smart Tumor Microenvironment-Responsive Nano-Prodrug for Disulfiram Toxification In Situ and the Exploration of Lethal Mechanisms in Cells. *Langmuir*. 2022;38(1):584–592. doi:10.1021/acs.langmuir.1c03256
46. Zhang J, Hu M, Wen C, et al. CeO_2 @CuS@PDA-FA as targeted near-infrared PTT/CDT therapeutic agents for cancer cells. *Biomed Mater*. 2023;18(6):065006. doi:10.1088/1748-605X/acf825